

THE RELATION BETWEEN WALL PRESSURE AND VELOCITY FLUCTUATIONS IN A TURBULENT SEPARATION BUBBLE

Sen Wang

Department of Mechanical Engineering
University of Alberta
Edmonton, AB
sen6@ualberta.ca

Bradley Gibeau

Department of Mechanical Engineering
University of Alberta
Edmonton, AB
bgibeau@ualberta.ca

Sina Ghaemi

Department of Mechanical Engineering
University of Alberta
Edmonton, AB
ghaemi@ualberta.ca

ABSTRACT

We investigated the relationship between velocity and wall-pressure fluctuations in a turbulent separation bubble formed just upstream of an airfoil trailing edge. The experiments were conducted at a chord-based Reynolds number of 720,000 and an angle of attack of 9.7°. Synchronized measurements of wall-pressure fluctuations and time-resolved planar particle image velocimetry were performed in a streamwise-wall-normal plane along the midspan of the airfoil. A turbulent separation bubble that was triangular in shape formed between two shear layers that emerged from the suction and pressure sides of the wing. The flow unsteadiness was characterized using the Strouhal number, St_t , defined based on the characteristic length of the separation bubble and freestream velocity. The results show that wall-pressure fluctuation upstream of the detachment correlates with the unsteadiness in the shear layer above the separation bubble at St_t of approximately 0.04. The positive and negative pressure fluctuations are related to the expansion and contraction of the TSB (i.e., the breathing motion) through variations of the adverse pressure gradient.

INTRODUCTION

Trailing-edge (TE) separation typically refers to the detachment of a turbulent boundary layer from the aft section of an airfoil due to an adverse pressure gradient. The separated flow forms a turbulent separation bubble that features an intermittent separation front and shear layers that roll up into spanwise vortices (Thompson and Whitelaw, 1985). The incoming turbulent boundary layer (TBL) contains high-frequency unsteadiness, while the separation bubble exhibits lower frequencies due to the vortex shedding and breathing motions (Mohammed-Taifour and Weiss, 2016). The latter motion results in the large-scale spatial variation of the turbulent separation bubble (TSB) and has been subjected to recent investigations (Weiss et al., 2015; Mohammed-Taifour and Weiss 2016; Le Floch et al., 2020).

Several explanations were proposed to address the low-frequency breathing motion and the hypotheses were mainly categorized into two groups based on the location of unsteadiness. One group attributed the breathing of the separation bubble to the unsteadiness downstream of the detachment point. Numerous studies pointed out that the instantaneous imbalance of the entrainment and reinjection of

fluid due to the propagation of vortices is responsible for low-frequency breathing (Eaton & Johnston, 1982; Na & Moin, 1998). Another group ascribed the breathing motion to the perturbations in the incoming flow. In the DNS of Wu et al. (2020), the breathing motion was attributed to Görtler-type instabilities upstream of the detachment by examining the low-frequency flow structures using dynamic mode decomposition. A recent experimental work by Mohammed-Taifour & Weiss (2021) provided further evidence by showing the suppression of TSB expansion through controlled perturbation in the upstream flow. Both groups of mechanisms were broadly investigated in geometry-induced and pressure-induced separation. However, it is still unclear whether these mechanisms are applicable in TE separation since the flow condition is more complex.

The low-frequency unsteadiness in a separated flow has a Strouhal number, St_t , that is several orders of magnitude lower than the fluctuations in the TBL, and the corresponding St_t is usually on the order of 0.01. This result is supported by numerous investigations of TSBs induced by pressure gradients on flat plates (Weiss et al., 2015; Mohammed-Taifour & Weiss 2016; Le Floch et al., 2020) and by forward-facing steps (Camussi et al., 2008; Graziani et al., 2018). There are also some documented results suggesting that low-frequency breathing features a St_t on the order of 0.1 (Eaton and Johnston 1982; Wu et al. 2020). The discrepancy in St_t is not well-understood and may be a result of varying flow conditions.

In the context of airfoil separation, several studies have hinted at a possible connection between the low-frequency breathing of the TSB and the force fluctuations on the airfoil by comparing their dominant St_t (Broeren & Bragg, 1998; Weiss et al., 2015, Liu & Xiao, 2020). It, therefore, seems pertinent to further investigate the unsteadinesses of TSBs if we wish to fully understand the vibration and noise associated with TE separation. In particular, investigating the relationship between the velocity field and wall-pressure fluctuations will improve our understanding of breathing motion and how it impacts airfoil performance.

The objective of the present investigation is to determine the relationship between the wall-pressure fluctuations and the flow motions in the vicinity of the separation bubble. The study was carried out using synchronized wall-pressure and time-resolved planar particle image velocimetry (PIV) measurements. The investigation provides insight into the

origin of the pressure fluctuations within different frequency bands.

EXPERIMENTAL SETUP

The present experiments were conducted in a two-story, closed-loop wind tunnel with a cross-section of $2.4 \times 1.2 \text{ m}^2$. A NACA 4418 airfoil was installed vertically in the wind tunnel at an angle of attack of 9.7° . The airfoil had a chord length of $c = 975 \text{ mm}$ and a span of 1190 mm . A tripwire was installed $0.2c$ downstream of the leading edge. The experiments were conducted at a freestream velocity (U_∞) of 11.2 m/s , which corresponds to a chord-based Reynolds number of $720,000$. The origin O of the coordinate system is located at the center of the trailing edge as shown in Figure 1(a). The streamwise, wall-normal, and spanwise directions are denoted by x , y , and z , respectively.

Time-resolved planar PIV measurements were conducted at the trailing-edge region of the airfoil. The measurements along the midspan in the x - y plane employed two high-speed cameras (Phantom v611). The stitched field of view, as shown by the blue dash-line boxes in Figure 1(a), was $500 \times 125 \text{ mm}^2$ ($x \times y$) with a digital resolution of 0.2 mm/pixel . An Nd:YLF laser (Photonics Industries DM20-527-DH) was used to illuminate the measurement plane. The data acquisition was performed at 2 kHz . In total, ten time-resolved datasets were collected; each set was 3.45 s . The signal-to-noise ratio of the PIV images was improved by removing the ensemble minimum and normalizing with the ensemble average. The vector fields were obtained by performing a sliding sum-of-correlation using three successive image pairs and a final interrogation window size of 32×32 pixels with 75% overlap.

Wall-pressure measurements were conducted simultaneously with the time-resolved PIV measurements using infrasound microphones (1/2-inch Brüel & Kjær 4964) paired with pre-amplifiers (Brüel & Kjær 2669). The microphones were calibrated using a constant-frequency calibrator (Brüel & Kjær 4231) at 1 kHz . The sampling frequency was set to 20 kHz , and the pressure signals were recorded using Simulink Real-Time through a Speedgoat Target Machine with a 16-bit input/output module (model IO135). The trigger signals of the PIV system were also recorded for the purpose of data synchronization in post-processing. The microphones were placed behind pinholes to avoid spatial filtering of the pressure signals. The wall-pressure measurements were carried out at seven streamwise locations along the midspan. A detailed view of the pinholes on the wing surface is shown in the zoomed-in view within Figure 1(a). The most upstream pinhole was at $x/c = -0.30$, and the most downstream pinhole was at $x/c = -0.08$. The spacing between the pinholes was approximately $0.035c$. The freestream velocity was carefully adjusted to have the mean separation point coincide with the pinhole at $x/c = -0.19$ such that there were three pinholes upstream and downstream of the mean separation point.

The cross-section views of the microphone installation in the wall-normal-spanwise and streamwise-wall-normal planes are provided in Figure 1(b) and (c), respectively; a local coordinate system is illustrated with its local origin O' at the center of the pinhole, on the wing surface. The local coordinate axes (x' , y' , and z') are in the same directions as those associated with origin O . As shown in Figure 1(b), the microphone is threaded into the dark grey region, and its diaphragm is highlighted by the blue line. A cylindrical cavity

with a radius of 5 mm and a depth of 3 mm is formed as shown in the light grey region in Figure 1(b) and (c). The pinhole has a length of 3.5 mm and a diameter of 0.5 mm that connects the cavity to the wing surface. The length of the pinhole is more than twice the size of its diameter, as suggested by Shaw (1960). The pinhole-cavity device acts as a Helmholtz resonator (Tsuji et al., 2007), resulting in amplitude and phase distortion. These distortions were corrected using the transfer function of the resonator which was determined using a dynamic calibration technique. A Wiener filter was employed to remove the wind tunnel background noise using an additional microphone placed in the freestream.

RESULTS AND DISCUSSION

In this work, the instantaneous velocities in the x and y -directions are denoted by U and V , respectively. The corresponding fluctuating velocity components are u and v , and the fluctuating wall pressure is p . An ensemble average in time is represented by $\langle \dots \rangle$ and the subscript 'rms' is used to indicate the root-mean-square value of a variable.

The power spectral density (PSD) of p/p_{rms} at various pinhole locations are presented in Figure 2. The Strouhal number St_l is defined as fl/U_∞ , where l is the characteristic length of the mean separation bubble. In this work, l is defined as the distance between the most upstream and downstream points of the mean TSB and is equal to $0.25c$. The PSDs upstream of the mean detachment point ($x/c = -0.19$) for the pressure sensors located at $x/c = -0.30$, -0.26 , and -0.23 are relatively flat until $St_l \approx 1$, followed by a rapid drop in power at higher St_l . For the pressure sensors located at $x/c = -0.16$, -0.12 , and -0.08 , a broad peak in the PSDs is present at $St_l \approx 0.3$. For these locations, the rapid decay of PSD starts at a lower St_l around 0.5 . With increasing x/c , the mid-frequency p appears to be stronger, and the high-frequency p is less significant. The results of Figure 3 generally agree with the observations of Weiss et al. (2015). In their work, they concluded that the high-frequency pressure fluctuations are related to small-scale turbulence fluctuations, the mid-frequency ($St_l = 0.2$ to 0.4) pressure fluctuations are induced by the flapping of the shear layer, and the low-frequency pressure fluctuations are associated with the breathing motion. In the present work, the difference in power between low-frequency and mid-frequency pressure fluctuations is not well pronounced as seen in the work of Weiss et al. (2015). The measured fluctuations in the TSB appear to be more energetic at $St_l \approx 0.3$, which suggests the flapping of shear layer may play a more important role in varying wall-pressure fluctuation.

A contour of normalized instantaneous velocity, U/U_∞ , is illustrated in Figure 3(a). The boundary of the TSB is indicated by the contour of $U = 0$ using black lines. The irregular upper border of the boundary in the x - y view is associated with the roll-up of the shear layer. The velocity field reveals the existence of two shear layers, developed along the suction and pressure surfaces of the wing. The contours of forward-flow probability, γ , are plotted in Figure 3(b). The mean boundary of the TSB generally overlaps with the contour of $\gamma = 0.5$. The upper and lower shear layers are identified using the local minimum and maximum of the mean spanwise vorticity ($\langle \Omega_z \rangle$), respectively. They are illustrated by the blue dashed lines in the figure. The two shear layers forge the triangular shape of the TSB.

Since the dynamics of the TSB are highly affected by the shear layers, we performed a spectral analysis of u along the upper shear layer to investigate the associated unsteadiness. The PSD of u/U_∞ as a function of x/c along the upper shear layer is shown in Figure 4(a). Energetic unsteadiness is visible downstream of the mean detachment point (i.e., $x/c > -0.2$) at $St_l < 0.04$. A secondary peak is also observed downstream of the TE (i.e., $x/c > 0$) at $St_l = 0.14$. The spectral analysis of flow unsteadiness in the upper shear layer reveals that the dominant peak is at $St_l = 0.04$, which is potentially related to the low-frequency breathing of the TSB.

To identify the relationship between wall-pressure fluctuation and the unsteadiness in the upper shear layer, the coherence function, C_{pu} , between p at $x/c = -0.30$ and u along the upper shear layer is investigated in Figure 4(b). The result shows that the highest local C_{pu} is observed at $St_l = 0.04$. This matches the dominant frequency of unsteadiness observed in Figure 4(a) and is similar to the frequency of the breathing motion reported in investigations of TSBs on flat plates (Weiss et al., 2015; Mohammed-Taifour and Weiss 2016; Le Floch et al., 2020). It also appears that C_{pu} downstream of $x/c = -0.30$ is much higher than upstream of $x/c = -0.30$. The dominant peak of C_{pu} is seen at $-0.03 < x/c < 0.09$. The fact that a strong coherence is detected downstream of the reference point suggests that the low-frequency pressure fluctuations generated by the shear layer unsteadiness propagate upstream of the mean TSB.

To identify the motions responsible for the low-frequency content in wall-pressure fluctuations, two-point correlations between low-pass-filtered p at $x/c = -0.30$ and fluctuating velocities (u and v) in the measured domain were performed. Based on the results of C_{pu} in Figure 4(b), a low-pass cut-off frequency at $St_l = 0.1$ (6.5 Hz) is used to extract the low-frequency content of p . The correlations are further separated using positive (superscript '+') and negative pressure (superscript '-') to isolate the motions associated with each sign of fluctuation. The correlations with $p < 0$ are multiplied by -1 to retain the true velocity directions in the visualizations. The correlations are described by

$$R_{pu}^+(\Delta x, \Delta y) = \frac{\langle p(t)u(\Delta x, \Delta y, t) \rangle}{p_{rms}u_{rms}} \Big|_{p>0}, \text{ and} \quad (1)$$

$$R_{pu}^-(\Delta x, \Delta y) = \frac{\langle p(t)u(\Delta x, \Delta y, t) \rangle}{p_{rms}u_{rms}} \Big|_{p<0}, \quad (2)$$

where R_{pu} is the streamwise component of the correlation coefficient. A similar correlation was carried out using p and v to obtain R_{pv} as the wall-normal component. The spatial correlations of R_{pu} associated with $p > 0$ and $p < 0$ are presented in Figure 5(a) and (b), respectively. The contour of $\langle U \rangle = 0$ is illustrated using a green line to show the position of the mean TSB. The results of Figure 5 demonstrate that low-frequency positive and negative p are correlated with large-scale streamwise flow motions downstream of the reference point ($x/c = -0.30$). In particular, the low-frequency positive p is correlated with a large-scale backward flow motion, i.e., low-frequency expansion of the TSB. The negative p correlates with the low-frequency forward flow motion, which is the contraction of the TSB. The breathing of the TSB can therefore increase/reduce the adverse pressure gradient upstream of the TSB, and produce low-frequency positive and negative pressure fluctuations, respectively.

It is of interest to note that the low-frequency positive and negative p do not show a strong correlation with any local

wall-normal flow motions as seen in the work of Gibeau & Ghaemi (2021), where the positive and negative p at the lowest frequencies are induced by wall-normal velocity associated with very-large-scale motions. The different observations reveal that there is a fundamental difference in the mechanisms that induce low-frequency positive and negative p in an attached TBL versus a TSB with breathing motions. The present result is more likely due to the effect of suction/compression above the pinhole created by the contraction/expansion of the TSB.

CONCLUSION

The present study demonstrated that the PSD of wall-pressure fluctuations in the TSB features a broad peak at $St_l = 0.3$. The high-frequency pressure fluctuation within the same region rapidly decayed with increasing St_l . The most energetic unsteadiness in the upper shear layer above the separation bubble was observed at $St_l = 0.04$. Through the investigation of the coherence between the unsteadiness in the upper shear layer and low-frequency wall-pressure fluctuation at $x/c = -0.30$, it was found that the low-frequency wall-pressure fluctuations upstream of the detachment point correlated with the unsteadiness in the upper shear layer at St_l of 0.04. The associated flow motion was identified as the breathing of the turbulent separation bubble. The positive and negative wall-pressure fluctuations were related to the expansion and contraction of the separation bubble through the variation of the adverse pressure gradient.

REFERENCES

- Broeren, A., & Bragg, M., 1998, "Low-frequency Flowfield Unsteadiness During Airfoil Stall and the Influence of Stall Type", *16th AIAA Applied Aerodynamics Conference*, Albuquerque, N.M., U.S.A., pp. 2517.
- Camussi, R., Felli, M., Pereira, F., Aloisio, G. & Dimarco, A., 2008, "Statistical Properties of Wall Pressure Fluctuations over a Forward-facing Step", *Phys. Fluids*, Vol. 20 (7), pp. 075113.
- Eaton, J. K., & Johnston, J. P., 1982, "Low Frequency Unsteadiness of a Reattaching Turbulent Shear Layer", *Turbulent shear flows 3*, Springer, Berlin, Heidelberg, pp. 162-170.
- Gibeau, B., & Ghaemi, S., 2021, "Low- and Mid-frequency Wall-pressure Sources in a Turbulent Boundary Layer", *J. Fluid Mech.*, Vol. 918.
- Graziani, A., Kerhervé, F., Martinuzzi, R.J. & Keirsbulck, L., 2018, "Dynamics of the Recirculating Areas of a Forward-facing Step", *Exp. Fluids*, Vol. 59 (10), pp. 154.
- Le Floch, A., Weiss, J., Mohammed-Taifour, A., & Dufresne, L., 2020, "Measurements of Pressure and Velocity Fluctuations in a Family of Turbulent Separation Bubbles", *J. Fluid Mech.*, Vol. 902.
- Liu J. & Xiao Z., 2020, "Low-frequency Oscillation over NACA0015 Airfoil Near Stall at High Reynolds Number", *AIAA Journal*, Vol. 58, pp. 53-60.
- Mohammed-Taifour, A., & Weiss, J., 2016, "Unsteadiness in a Large Turbulent Separation Bubble", *J. Fluid Mech.*, Vol. 799, pp. 383-412.
- Mohammed-Taifour, A., & Weiss, J., 2021, "Periodic forcing of a large turbulent separation bubble", *J. Fluid Mech.*, Vol. 915.

Na, Y., & Moin, P., 1998, "Direct Numerical Simulation of a Separated Turbulent Boundary Layer", *J. Fluid Mech.*, Vol. 374, pp. 379-405.

Shaw, R., 1960, "The Influence of Hole Dimensions on Static Pressure Measurements", *J. Fluid Mech.*, Vol. 7, pp. 550-564.

Thompson, B. E., & Whitelaw J. H., 1985, "Characteristics of a trailing-edge flow with turbulent boundary-layer separation", *J. Fluid Mech.*, Vol. 157, pp. 305-326.

Tsuji, Y., Imayama, S., Schlatter, P., Alfredsson, P. H., Johansson, A. V., Marusic, I., Hutchins, N. & Monty, J. 2012, "Pressure Fluctuations in high-Reynolds-number Turbulent Boundary Layer: Results from Experiments and DNS", *J. Turb.*, Vol. 13 (50), pp. 1-19.

Weiss, J., Mohammed-Taifour, A., & Schwaab, Q., 2015, "Unsteady Behavior of a Pressure-Induced Turbulent Separation Bubble", *AIAA Journal*, Vol. 53(9), pp. 2634-2645.

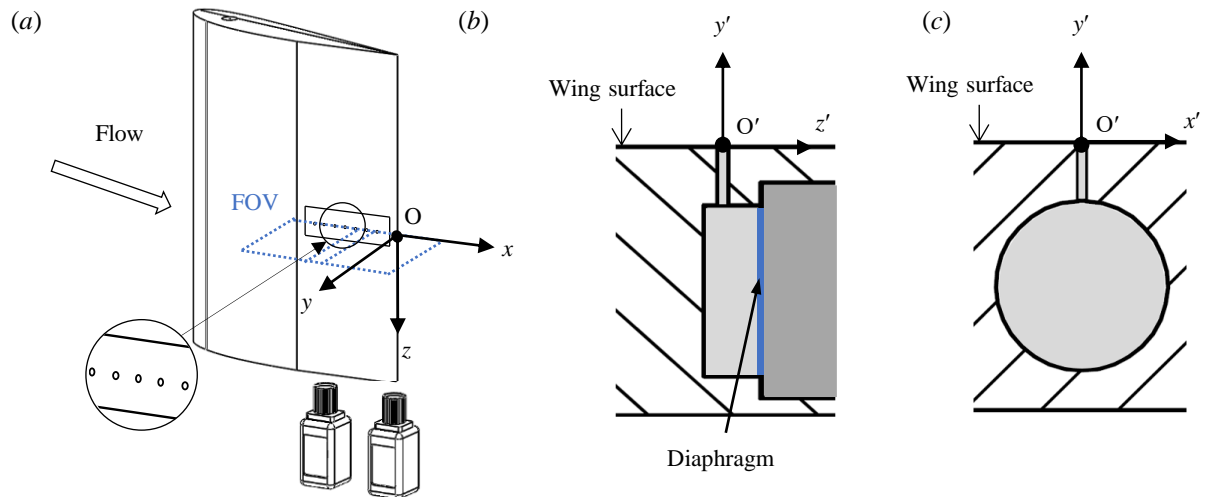


Figure 1. (a) Schematics of the time-resolved planar PIV where the combined FOV is represented by the blue dash-line boxes. The cross-section views of the microphone installation in (b) the streamwise-spanwise, and (c) streamwise-wall-normal plane.

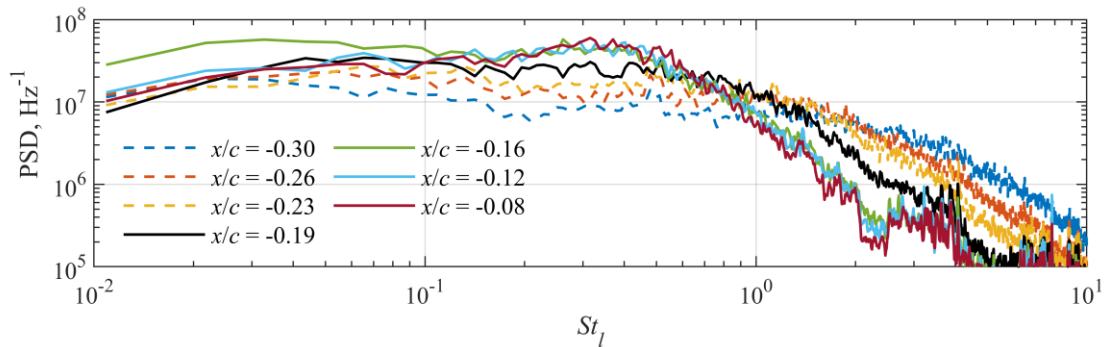


Figure 2. PSD of p/p_{rms} at seven streamwise locations along the centreline of the 2D wing.

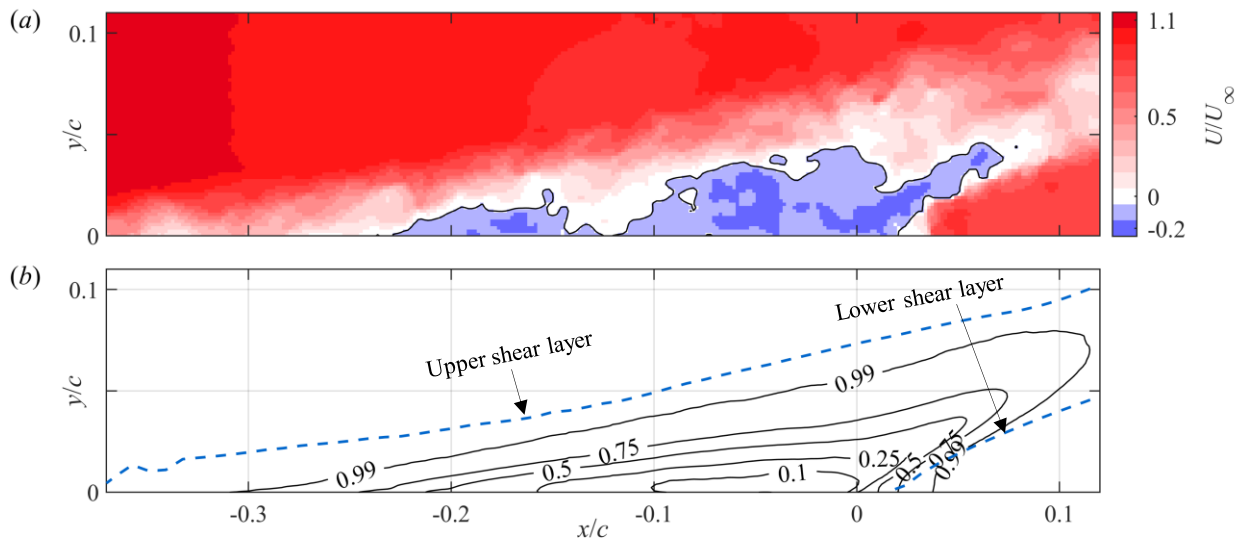


Figure 3. (a) Sample contours of U/U_∞ with the TSB boundary, represented by the contour of $U = 0$, shown in black lines. (b) The contours of the forward-flow probability γ are presented using black lines. The wall-normal locations of $\langle \Omega_z \rangle_{\min/\max}$ as a function of x/c are shown using blue dashed lines to represent the upper and lower shear layers.

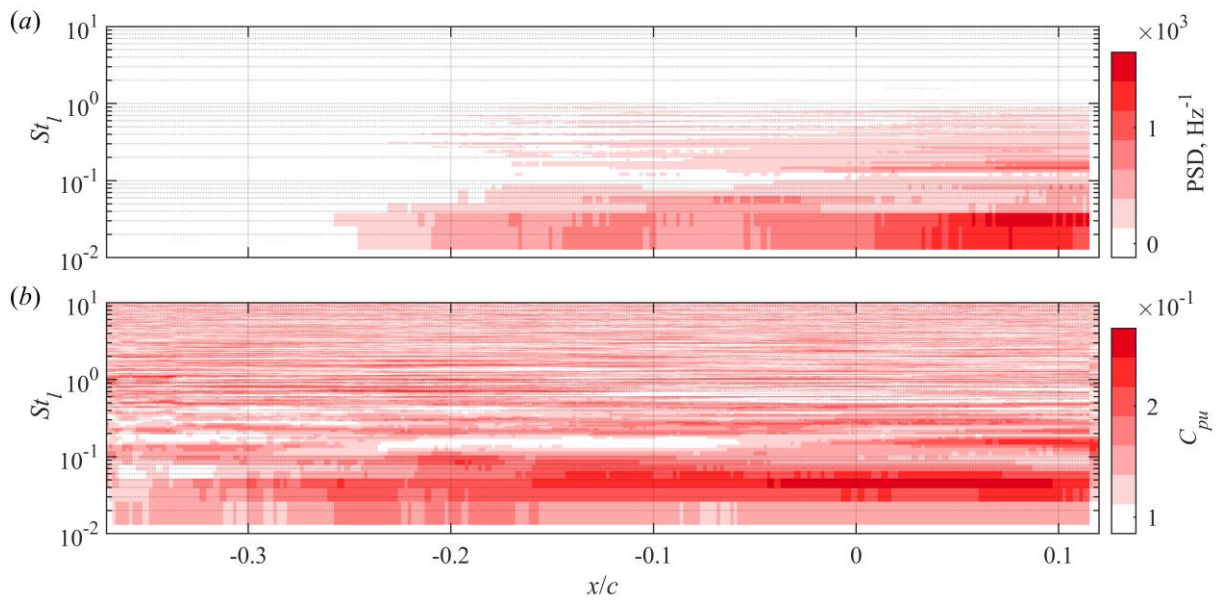


Figure 4. (a) The contours of PSD of u/U_∞ in the upper shear layer. (b) The coherence C_{pu} between p at $x/c = -0.30$ and u from the upper shear layer.

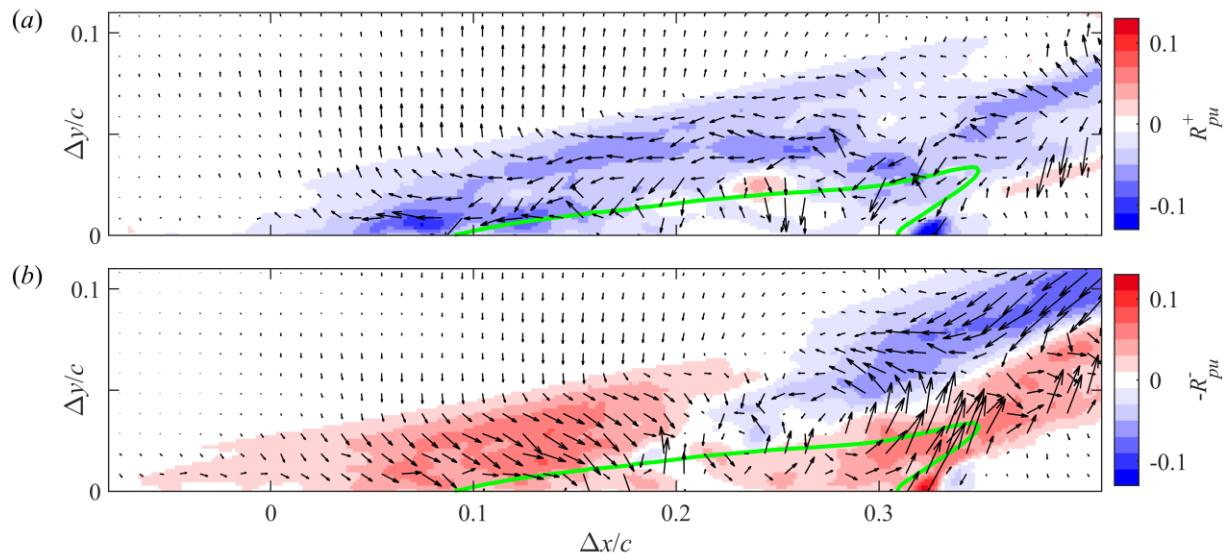


Figure 5. Visualizations of the pressure-velocity correlations associated with (a) $p > 0$ and (b) $p < 0$. A low-pass filter of $St_l < 0.1$ was applied to extract the low-frequency p before computing the correlations. The reference point of p is at $x/c = -0.30$ on the wall and is represented by $\Delta x = 0$ here. The vector field is constructed using R_{pu} and R_{pv} . An overlay of the contour of $\langle U \rangle = 0$ (green line) is added to show the position of the mean TSB.